Structure, shape and dynamics of biological membranes.

Idema, T.

Citation

Idema, T. (2009, November 19). *Structure, shape and dynamics of biological membranes*. Retrieved from https://hdl.handle.net/1887/14370

CHAPTER 5

MEMBRANE MEDIATED INTERACTIONS

The organization of the membrane in a living cell is the result of the collective effect of many driving forces. Several of these, such as electrostatic and Van der Waals forces, have been identified and studied in detail. In this chapter we investigate and quantify another force, the interaction between inclusions via deformations of the membrane shape. For electrically neutral systems, this interaction is the dominant organizing force. We use the domains in phase separated ternary vesicles as probes to study membrane mediated interactions. Once domains partially bud out from the mother vesicle, they deform their surroundings and start interacting. We show that this partial budding can only occur in a stretched membrane, where the vesicle surface is in the elastic regime. The membrane mediated interactions that appear as a consequence of this partial budding process, lead to a kinetically arrested state in which coarsening is significantly slowed down. Consequently, we find that long range order and a preferred domain size naturally appear in our system. We quantify the interactions between the domains, both in experiments and in the context of our theoretical model, and obtain the domain size distributions from Monte Carlo simulations.

5.1 Introduction

As described in chapter 3, a ternary vesicle below its critical temperature will quickly nucleate domains of one (typically L_o) liquid phase in a background of another phase (typically L_d). When there is no pressure gradient across the membrane, the vesicle as a whole is spherical and the nucleated domains can freely diffuse on its surface. They grow by coalescing, and relatively quickly all merge into one large domain. Allowing the vesicle to relax its enclosed volume (by waiting for several days or even weeks), the resulting shape is the 'snowman' we studied in chapter 4. This equilibrium shape can be understood as a trade-off between the elastic energy of the membrane and the line tension on the domain boundary.

When we put a pressure gradient across the membrane before quenching the vesicle below its critical temperature, the dynamics and resulting shape are quite different. Because the vesicle very quickly reduces its enclosed volume in order to counter the pressure gradient, there is some excess membrane area compared to the pressure-neutral case. Domains that have grown beyond a certain minimal size (set by the *invagination length* ξ [69], the ratio of the bending modulus and the line tension), can gain free energy by partially budding out from the vesicle, reducing the length of their domain boundary. The energy due to the line tension term then gets reduced, but the elastic bending energy increases, suggesting another trade-off equilibrium. However, as Lipowsky already showed [69], a model with just these two ingredients results in either no budding at all for weak line tensions, or complete budding for strong line tensions. We study this system in section 5.3 and show that partial budding can be explained by including the energy contribution due to membrane stretching.

Domains that partially bud do not only deform themselves, but also the membrane around them. Such deformations lead to an effective interaction between the domains through the differential curvature they impart. These membrane-mediated interactions have recently attracted the attention of several groups [97–104]. They turn out to be repulsive between like inclusions, and lead to the formation of kinetically arrested patterns of domains [6, 105, 106]. Vesicles with such patterns of domains are said to exhibit microphase separation: the domains are phase separated, but the vesicle as a whole is not. Microphase separation is a metastable state (the ground state is still the fully phase-separated vesicle of chapter 4), however, it persists for biologically relevant time scales. Microphase separated vesicles are moreover an ideal model system to study the interactions of other membrane inclusions such as curvature-inducing proteins [97, 99, 103, 107]. Working with domains carries two great advantages over using actual proteins. Firstly, the domains interact only through the membrane shape deformations they induce. Secondly, they are straightforward to visualize and track.

In this chapter, we study the properties of the membrane-mediated interactions between many L_o domains on a L_d background in a ternary membrane vesicle. We measure the distribution of domain sizes and find a pronounced preferred length scale. By analysis of the fluctuations of domain positions we quantify the strength of membrane interactions and find a nontrivial dependence of the interaction strength on domain size. Those effects are captured qualitatively in a simple model. Our findings shed new light on intramembrane interactions between protein patches. Moreover, they also yield new information on the domain size distribution and the stability of microphase separation in multicomponent biomimetic membranes.

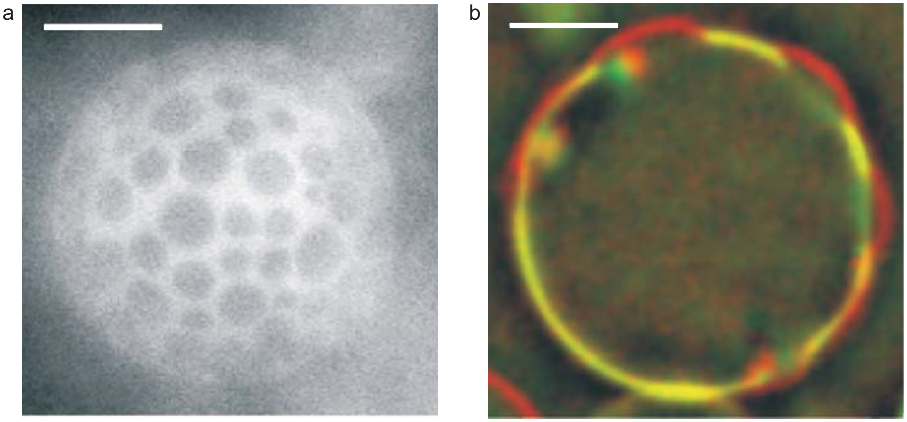

Figure 5.1: Typical example of a partially budded vesicle. (a) Complete vesicle, the L_d phase is stained and appears bright, the dark spots are L_o domains. (b) Cross-section, overlay of $405\ \mathrm{nm}$ excitation (perylene, red) and $546\ \mathrm{nm}$ excitation (rhodamine, yellow). Both scalebars: $20\ \mu\mathrm{m}$.

5.2 Evidence for interactions

The experimental data presented in this chapter is once again due to S. Semrau from the Leiden University experimental biophysics group, and used with permission; see appendix 4.A for experimental details. The experimental system considered in this chapter consists of a ternary GUV with many L_o domains in a L_d background, see figure 5.1a. After preparation by means of electroformation the vesicles have a spherical shape. By increasing the osmotic pressure outside the vesicle we produce a slight increase in surface to volume ratio. For this reason some of the vesicles show partially budded L_o domains, see figure 5.1b. Those domains posses long term stability (see Movie S1 of [71]; in experiments we observed stability on the time scale of several hours). In contrast, ‘flat’ domains, which have the same curvature as the vesicle as a whole, rapidly fuse until complete phase separation is attained [70, 106].

The stability of the vesicles with budded domains indicates that the domains experience a repulsive interaction that prevents them from merging. This interaction also affects the distribution of domain distances (radial distribution function) and domain sizes.

5.2.1 Radial distribution function

Figure 5.2 shows the radial distribution function (rdf) of the center-to-center distance of domains for a typical vesicle. The rdf gives the probability of finding a domain a distance d away from an arbitrary chosen central domain. The first (and highest) maximum in the rdf corresponds to the first coordination shell, *i.e.*, the nearest neighbors. The distance between nearest neighbors is denoted by a. On average $a = 9$ μm, while the radius of a domain is on average 3 μm and the vesicle radius equals 34 μm on average. Figure 5.2 clearly shows two additional maxima roughly at $2a$ and $3a$ which correspond to the second and third coordination shell. The rdf therefore indicates that the domains are not randomly distributed, but that instead their positions are correlated. Consequently the system of diffusing domains can be characterized as a two-dimensional liquid with interactions. Since a exceeds the typical domain radius by a factor of 3, this interaction is different from mere hard core repulsion between the domains.

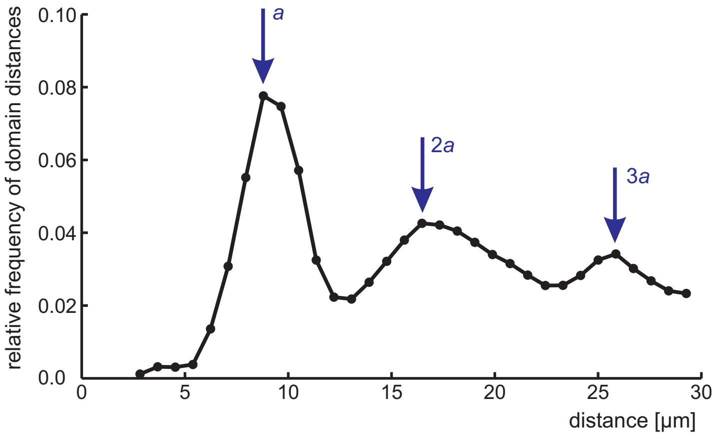

Figure 5.2: Typical radial distribution function for the center-center distances of the domains on a single vesicle. The nearest neighbor distance is denoted by a.

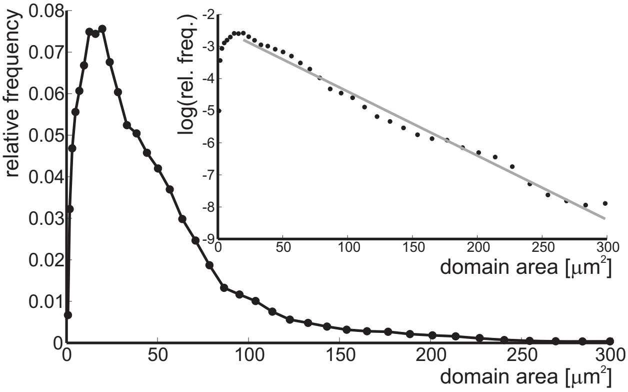

Figure 5.3: Distribution of domain sizes on all 24 vesicles. Inset: a logarithmic plot of the domain size distribution shows that it exhibits an exponential decay towards large domains (solid line).

5.2.2 Size distribution

Figure 5.3 shows the combined domain size distribution of all observed vesicles. The distribution is not uniform, but instead shows an absolute maximum, corresponding to a preferred domain size. Moreover, there is a long tail to larger domain sizes which drops off exponentially, as can be seen in a logscale plot (figure 5.3 inset). This nonuniform distribution can be understood in a picture that includes both domain fusions and domain interactions.

As was already reported by Yanagisawa *et al.* [106], we find that domains fuse when they are small. However, due to the repulsive interaction, which increases in strength when domains grow larger, the fusion of domains becomes kinetically hindered and slows down significantly with increasing domain size. When the repulsive interaction has grown to the size of the thermal energy ($k_B T$), the fusion process has slowed down considerably and the vesicle with multiple domains enters the metastable, kinetically arrested state which we observe in the experiments.

The exponential tail we find in the domain size distribution is a direct consequence of the finite total domain area. We expect to find such a tail both with and without interactions between the domains, as can be easily seen from a simple master equation description of the system (see appendix 5.A). We note that the master equation approach breaks down when the total number of domains becomes small, but since the experimental vesicles typically have several hundreds of domains, we are well within the validity range of this description. Without interactions between the domains, we find that the distribution of domain sizes is purely exponential and decays quickly, until ultimately a single domain remains. In the experimental data shown in figure 5.3 however, there is a distinct peak in the distribution around domains of about $25\ \mu\mathrm{m}^2$ in area, or $3\ \mu\mathrm{m}$ in radius. Moreover, the distribution remains stable on timescales much longer than it takes for flat domains to all merge. Both these observations suggest the presence of a repulsive force between the domains, hindering their fusion. To verify the claim that such a repulsion gives the observed size distribution, we performed Monte Carlo simulations of domain coalescence. The details of these simulations are given in appendix 5.B. The results of the simulations, both with and without interactions between the domains, are plotted in figure 5.4. As expected, the exponential tail in the domain size distribution is reproduced by both simulations. However, the absolute maximum in the experimental data is only reproduced in the simulations which include an interaction between the domains. Moreover, when interactions are present, we find that at $T_{\mathrm{MC}} \approx 175$ phase separation is still not complete. This relaxation time is much longer than the time we found for complete phase separation in the case without interactions ($T_{\mathrm{MC}} \approx 2$). The Monte Carlo simulations therefore show that microphase separation is a quasistatic case which can be explained by assuming a repulsive force between the domains.

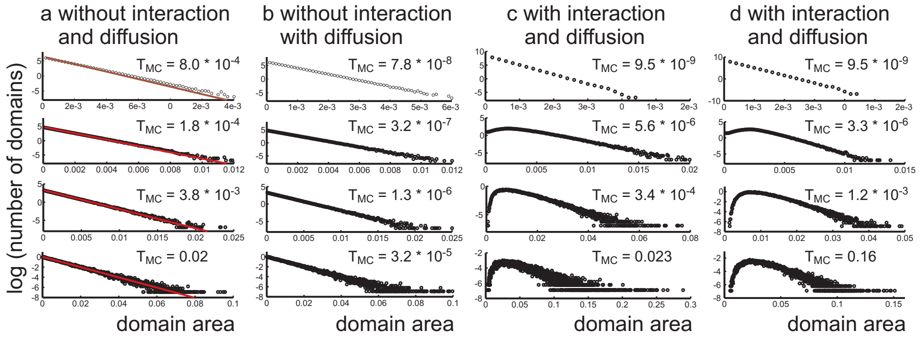

Figure 5.4: Domain size distributions determined using Monte Carlo simulations. All plots show the distribution for four different Monte Carlo times averaged over 1000 simulation runs (open circles). The initial condition is a random distribution of 10^4 domains of area $\varepsilon = 10^{-4}$. (a) Simulation without interactions and without diffusion. The gray line shows an exponential fit. (b) Simulation without interactions but including diffusion of domains. (c) Simulation including both domain diffusion and interactions; here $p_{i,j}^{\mathrm{merge}} = 10^{-6}/\sqrt{i * j}$. (d) Simulation including both domain diffusion and interactions; here $p_{i,j}^{\mathrm{merge}} = 10^{-6}/(i * j)$.

5.3 Domain budding

The experimentally observed distributions of domain distances and sizes can be explained by a repulsive membrane mediated interaction between the domains. Domains that partially bud out from the vesicle locally deform the membrane around them. Placing two budded domains close together causes this deformation to be larger, carrying a larger energy and resulting in an effective force between them. This membrane mediated force is therefore a direct consequence of the fact that the domains *partially* bud out from the vesicle. In this section we analyze the energetics of this partial budding process.

The first systematic study of domain budding was performed by Lipowsky in 1992 [69]. He modeled the domains as either circular disks in, or spherical caps on, a flat background. Domain budding is then a consequence of a trade-off between two competing forces, which we will treat here in a coarse-grained, mean-field manner. For a more detailed view on the microscopic processes involved we refer to reviews by Lipowsky *et al.* [108] and Seifert [109]. The first force is the line tension between the L_o domain and the L_d background, which favors budding because it reduces the length of the domain boundary. On the other hand the bending energy of the L_o domain resists budding because a budded domain has a higher curvature. Lipowsky found that there is a critical domain size at which there is a transition between an unbudded state and a fully budded domain. This lengthscale is called the *invagination length*, given by $\xi = \kappa_\mathrm{o}/\tau$, with κ_o the bending modulus of the L_o phase and τ the line tension on the domain boundary; in our experimental vesicles we have $\kappa_\mathrm{o} \sim 8.0 \cdot 10^{-19}$ J and $\tau \sim 1.2$ pN, giving $\xi \sim 0.7\,\mu\mathrm{m}$ (see chapter 4). The invagination length therefore sets the length scale at which we expect to find the first occurrence of domain budding. Although we occasionally see domains splitting off from the vesicle completely, we mostly observe partially budded domains. In the model proposed by Lipowsky partial budding is not possible, suggesting that we need to consider additional constraints on, for example, the vesicle area and volume, and/or additional energy contributions. Such constraints were also studied by Jülicher and Lipowsky [52,82]. They used numerical methods to find the minimal-energy shape of a L_d vesicle with a single L_o domain. Their results confirm the finding by Lipowsky that there is a critical domain size for budding. Moreover, they found that a constraint on the volume of the vesicle only changes the budding point but does not modify the qualitative budding behavior. In the following we show that it is not sufficient to just include area and volume constraints to explain the shape of our experimental vesicles. If we also allow for stretching of the membrane, we do get the partially budded vesicle shapes.

In general, the equilibrium shape of the membrane of a GUV is found by minimizing the associated shape energy functional under appropriate constraints on the total membrane area and enclosed volume, as explained in detail in section 2.3.5. The functional is composed of several contributions, reflecting the energy associated with the deformation of the membrane and the effect of phase separation of the different lipids into domains. The contribution due to bending of the membrane (the bending energy) is given by the Canham-Helfrich energy functional, equation (2.78):

$$\mathcal{E}_{\text{curv}} = \mathcal{E}_{\text{mean curv}} + \mathcal{E}_{\text{Gauss}} = \int_{\mathcal{M}} \left(\frac{\kappa}{2}(2H)^2 + \bar{\kappa} K \right) \mathrm{d}S. \tag{5.1}$$

Here H and K are the mean and Gaussian curvature of the membrane respectively, and κ and $\bar{\kappa}$ the bending and Gaussian moduli. Using the Gauss-Bonnet Theorem from section 2.3.4, we find that the integral over the Gaussian curvature over a continuous patch of membrane, such as one of our L_o domains or the L_d background, yields a constant bulk contribution (which we can disregard) plus a boundary term.

For a GUV with a uniform membrane, the shape that minimizes the bending energy (5.1) is found to be a sphere. If the membrane contains domains with different bending moduli κ, the sphere is no longer the optimal solution. However, within the bulk of each domain, far away from any domain boundary, the sphere is still a good approximation of the actual membrane shape (see section 4.3). For the case at hand, where we have many small and relatively stiff domains in a more flexible background, we follow Lipowsky [69] and model the small domains as spherical caps on a vesicle which also has spherical shape itself (see figure 5.5d). Although this model has the serious shortcoming that it suggests infinite curvature at the domain edge, it remains a good approximation for the overall vesicle shape, because it corresponds to the minimal-curvature solution of the shape equation on the entire vesicle except a few special points. For the special case that all domains are equal in size, we can describe them with a curvature radius R_c and opening angle θ_c, and the background sphere with its radius R_b and opening angle θ_b (see figure 5.5d). For the mean curvature energy of a system with N domains we then have

$$\mathcal{E}_{\text{mean curv}} = 4\pi\kappa_\text{o} N(1 - \cos\theta_c) + 4\pi\kappa_\text{d}(2 - N(1 - \cos\theta_b)), \tag{5.2}$$

where κ_o and κ_d are the bending moduli of the L_o and L_d phases respectively. The Gaussian curvature contribution is given by the boundary term

$$\mathcal{E}_{\text{Gauss}} = 2\pi N \Delta\bar{\kappa} \cos\theta_c, \tag{5.3}$$

with $\Delta\bar{\kappa}$ the difference in Gaussian curvature modulus between the L_o and L_d domains. As mentioned above, we model the fact that the lipids separate into two phases by assigning a line tension to the phase boundary (equation (2.102), see also section 3.4). The energy associated with that line tension τ in the spherical cap model is given by

$$\mathcal{E}_{\text{tens}} = 2\pi\tau N R_b \sin\theta_b. \tag{5.4}$$

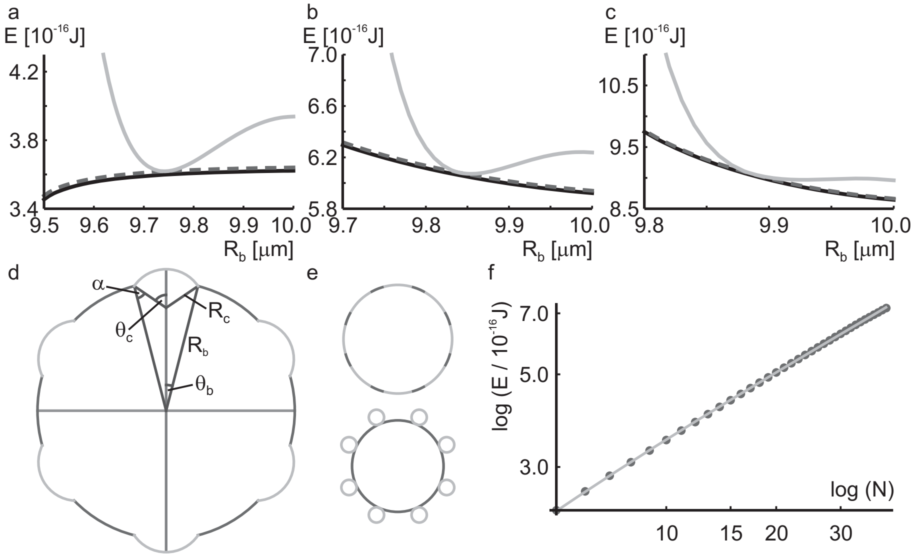

Figure 5.5: Coordinates and energy plots of the sphere-with-domains system. Energies are plotted for 10 (a), 25 (b) and 50 (c) domains as a function of the radius R_b of the background sphere. In each case the geometrical (5.5) and volume constraint (5.6) are met and the total area of the domains is fixed. The vesicles have an excess area fraction $(R_A - R_V)/R_V$ of 0.012. For the material parameters we use the values we obtained in chapter 4. The black solid line shows just the contributions of curvature and line tension; the dashed gray line those plus a surface tension term, and the gray solid line all contributions including a surface elasticity term (5.11). Without the surface elasticity term, the minimum of the energy is located at the maximum vesicle radius (figures b and c), implying flat domains (figure e top), or the minimum vesicle radius (figure a), implying full budding (figure e bottom). In the case of 50 domains the line tension energy per domain is not large enough to create buds. However, when there are only 25 domains, the line tension forces them to bud out and form spherical caps. (d) Coordinate system for the spherical caps model. (e) The two extremal situations - complete budding (bottom) and no budding at all (top). (f) Minimum of the energy (5.11) as a function of the number of domains. From the logarithmic plot shown here we find that the total energy as a function of the number of domains behaves as a power law with exponent 0.53.

If the total number N of domains is fixed, the energy given by the sum of equations (5.2), (5.3) and (5.4) is a function of four variables: R_b, R_c, θ_b, and θ_c. These variables are not independent, since they are subject to constraints. The first is that the membrane must be continuous at the domain boundary, which gives the geometric constraint

$$R_c \sin\theta_c = R_b \sin\theta_b. \tag{5.5}$$

Since the volume of the vesicle changes only over long timescales (hours) [110], we assume it is constant in our experiment (minutes), leading to a volume constraint on our system

$$\frac{4\pi}{3}\left[R_b^3 + NR_c^3(1-\cos\theta_c)^2(2+\cos\theta_c) - NR_b^3(1-\cos\theta_b)^2(2+\cos\theta_b)\right] = V_0, \tag{5.6}$$

where V_0 is the volume of the vesicle. Finally we consider the area of the vesicle. We have to treat the (total) area of the domains and that of the bulk phase separately. If we fix both of them, we obtain two additional constraints:

$$2\pi NR_c^2(1-\cos\theta_c) = A_{c,0}, \tag{5.7}$$

and

$$2\pi R_b^2(2-N(1-\cos\theta_b)) = A_{b,0}. \tag{5.8}$$

If all four constraints given by equations (5.5)-(5.8) are imposed rigorously, the shape of the vesicle is fixed, because there were only four unknowns in the system. For an experimental system at temperature $T > 0$ however, the total area is not conserved. Thermal fluctuations cause undulations in the membrane, resulting in a larger area than the projected area given by $A_{c,0}$ and $A_{b,0}$ [111]. For $T > 0$ we should therefore not work in a fixed-area ensemble, but rather in a fixed surface-tension ensemble. We drop the constraints given by equations (5.7) and (5.8) and instead add an area energy term to the total energy

$$\mathcal{E}_{\text{area}} = 2\pi\sigma_{\text{o}}NR_c^2(1-\cos\theta_c) + 2\pi\sigma_{\text{d}}R_b^2(2-N(1-\cos\theta_b)), \tag{5.9}$$

with σ_{o} and σ_{d} the surface tensions of the L_{o} and L_{d} phases respectively. Note that equation (5.9) can be interpreted in two ways: in the fixed area ensemble, it contains two freely adjustable Lagrange-multipliers (σ_{o} and σ_{d}) which enforce the conditions given by equations (5.7) and (5.8). In the fixed surface tension ensemble, σ_{o} and σ_{d} are set and the shape is found by minimizing the total energy with respect to the free parameters, considering the remaining geometrical and volume constraints given by equations (5.5) and (5.6). These constraints can of course be included in the total energy using Lagrange multipliers as well. This is often done for the volume constraint, and the associated Lagrange multiplier is usually identified as the pressure difference across the membrane. We stress that since we fix the total volume (*i.e.*, work in a fixed volume ensemble), this pressure is selected by the system and is not an input parameter. The Lagrange-multiplier approach is mathematically equivalent to imposing an external volume constraint as we do here for practical purposes.

Equation (5.9) correctly gives the free energy contribution of the area energy in what is called the entropic regime, where the dominant contribution to the area term is due to the thermal fluctuations of the membrane [111]. To account for the fact that the membrane itself can be stretched or compressed away from its natural area A_0, we include a quadratic term in the area of the membrane [112]

$$\mathcal{E}_{\text{elastic}} = \gamma \left(\frac{A - A_0}{A_0} \right)^2 . \tag{5.10}$$

The elastic modulus γ is approximately 10^{-14} J in the ternary system considered here [110]. One way to understand equation (5.10) is that in the high-tension or elastic regime, the surface tension is no longer a fixed number, but itself depends linearly on the area [111]. The total shape energy is given by the sum of the five contributions given by equations (5.2), (5.3), (5.4), (5.9), and (5.10)

$$\mathcal{E} = \mathcal{E}_{\text{mean curv}} + \mathcal{E}_{\text{Gauss}} + \mathcal{E}_{\text{tens}} + \mathcal{E}_{\text{area}} + \mathcal{E}_{\text{elastic}}. \tag{5.11}$$

With the constraints (5.5) and (5.6), we are left with two independent variables for the minimization of the total energy. Since the surface tension and elastic modulus of the L_{o} phase are much larger than that of the L_{d} phase [70, 110], we further assume that the area of the L_{o} domains is fixed. This leaves us with a single variable minimization problem, which we solve numerically. For the material parameters we use the values we obtained in the study of the fully phase-separated vesicles in chapter 4. In order for buds to be able to form, the vesicle needs to have some excess area, which we express by the excess area fraction $(R_A - R_V)/R_V$. Here $R_A = \sqrt{A/(4\pi)}$ and $R_V = (3V/(4\pi))^{1/3}$, with A the total vesicle area and V its volume. The results of the minimization of equation (5.11) are shown in figure 5.5a-c. In the same figures we plot the energy without the membrane stretching term (5.10). In this case we find no partial budding, showing that the area elasticity term is required to reproduce the experimental results, and that our experimental vesicles are well within the elastic regime. Plotting the minima of the energy as a function of the number of budded domains on the vesicle, we find that it decreases with the number of domains (figure 5.5f). Therefore the fully phase-separated vesicle is the ground state, as we expected from the fact that the line tension is strong enough to dominate the shape.

5.4 Measuring the interactions

5.4.1 Domain position tracking

In order to determine quantitatively the interaction strength between the domains, we tracked their positions over time. In particular, we regarded situations like the one shown in figure 5.6a, in which a single domain is surrounded and held in place by a shell of 4 to 6 neighbor domains. We recorded the distance between the central domain and the center of mass of the shell domains (projected on the vesicle surface) over time and calculated the mean squared displacement (msd), see figure 5.6a for a typical example. Using only relative distances eliminates any influence of putative flow or overall movement of domains.

Although the precise form of the potential that confines the central domain is not known, we can approximate it around the local minimum by a harmonic potential $U(x) = \frac{1}{2}kx^2$ with spring constant k, where x is the distance from the center of mass of the nearest neighbors. If we treat the domain as a random walker with diffusion constant D, our model is formally equivalent to an Ornstein-Uhlenbeck process [113]. Alternatively, one can imagine all domains connected by harmonic springs. This approach also leads to an isotropic harmonic confining potential for the central domain. The msd of the domain is then given by:

$$\langle \Delta x^2(\Delta t) \rangle = \frac{4k_{\mathrm{B}}T}{k}\left[1 - \exp\left(-\frac{kD}{k_{\mathrm{B}}T}\Delta t\right)\right] \approx 4D\Delta t \quad \text{for small } \Delta t. \tag{5.12}$$

In practice, we determined the diffusion coefficient D (and a small offset due to the finite positional accuracy) from a linear fit to the first 3 time lags (see figure 5.6a), since the reliability of the data points is highest in that region. The inset of figure 5.7 shows the diffusion coefficient as a function of the size of the central domain. The other parameter of the Ornstein-Uhlenbeck model (5.12) for the msd of a domain is the spring constant k. We determined its value from a fit of equation (5.12) to the full experimental data set, where D was fixed to the value determined before. Figure 5.7 shows k normalized by the number of nearest neighbors as a function of the size of the central domain. On average $k = 1.4 \pm 0.5\, k_{\mathrm{B}}T/\mu\mathrm{m}^2$. This value supports the observation that domains are stable over extended periods of time: since the distance between domains is typically several $\mu\mathrm{m}$ the energy barrier that the domains have to overcome in order to fuse is well above $k_{\mathrm{B}}T$. Due to the limited amount of available trajectories, the error in the determination of k is fairly large. Hence it is not possible to deduce the quantitative dependence of k on the domain size. Therefore we determined k more precisely in a separate, independent way, based on domain distance statistics.

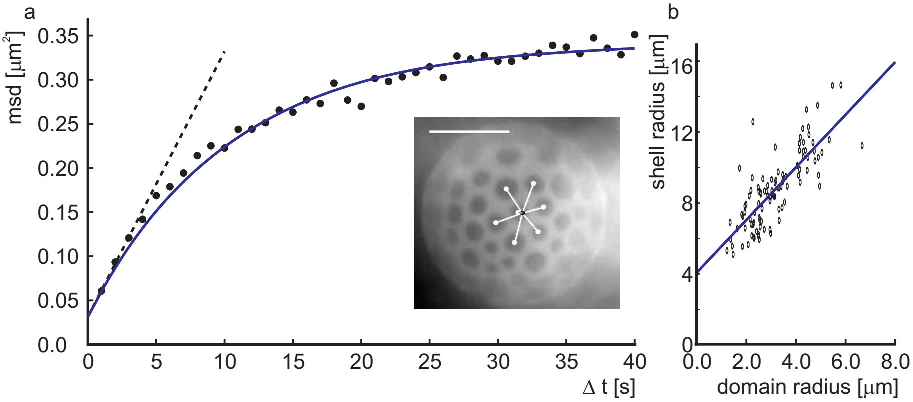

Figure 5.6: Domains caged in a shell of neighbors. (a) Typical example of the mean square displacement (msd) of the distance between a central domain and the center of mass of the surrounding domains (dots). The solid line is a fit to the Ornstein-Uhlenbeck model given by equation (5.12), the dashed line a linear fit to the first three data points, which we use to determine the diffusion coefficient. The inset shows an example of the tracking configuration. The centroids of the domains are indicated by white dots, and the center of mass of the six domains in the shell by a black dot. The distance between the centroid of the central domain and the center of mass is indicated by the gray line. The mean square displacement of this distance is used to determine the diffusional behavior of the central domain. Scalebar $20\ \mu\mathrm{m}$. (b) Shell radius versus central domain radius, the solid line corresponds to a linear fit with slope 1.5 and offset $4.1\ \mu\mathrm{m}$.

5.4.2 Domain distance statistics

The interaction potential between two domains can be directly inferred from the distribution of domain distances, as already demonstrated by Rozovsky *et al.* [105]. We consider a central domain surrounded by N nearest neighbors, whose combined imposed potential is given by $U(x)$. Then the probability $p(x)$ to find the central domain a distance x from the center of mass of the neighbors is proportional to the Boltzmann factor $p(x) \propto \exp\left(-\frac{U(x)}{k_\mathrm{B}T}\right)$. As before we assume the imposed potential, at least locally, to be harmonic, $U(x) = \frac{1}{2}kx^2$, which gives for $p(x)$:

$$-\log\left(p(x)\right) = \mathrm{const.} + \frac{1}{2}kx^2. \tag{5.13}$$

In order to determine k, we used (5.13) to fit $-\log\left(p(x)\right)$. We determined $p(x)$ from the distances of the 4 nearest neighbors of each domain, where we binned the data according to the size of the central domain. Figure 5.8 shows an example of the distance distribution and a fit of the potential to $-\log(p(x))$.

The available data set for domain distances is much larger than the one we obtained from domain tracking. Consequently, the spring constant k can be determined with a smaller error, see figure 5.9. The average $k = 1.6 \pm 0.2\, k_{\mathrm{B}}T/\mu\mathrm{m}^2$ coincides with the result found from domain tracking $k = 1.4 \pm 0.5\, k_{\mathrm{B}}T/\mu\mathrm{m}^2$. Interestingly, k shows a a nonlinear behavior with a clear maximum for domains of an intermediate size which roughly coincides with the size of the most abundant domains, see figure 5.3.

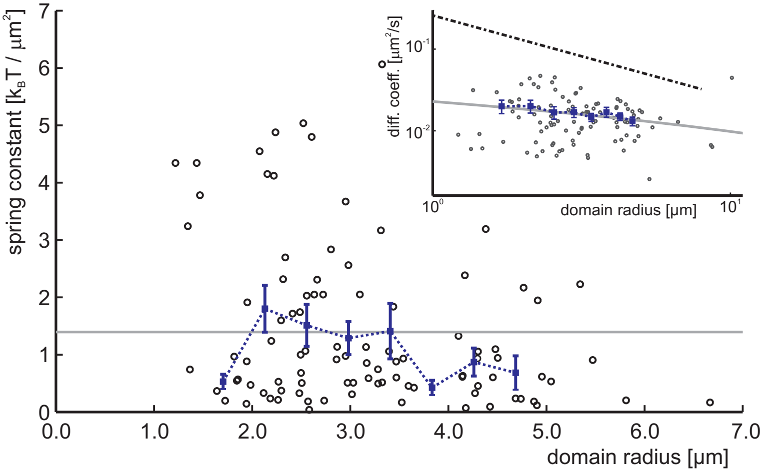

Figure 5.7: Spring constant k corrected for the number of nearest neighbors versus domain radius (circles), the squares correspond to binned data. The gray solid line marks the average $k = 1.4 \pm 0.5\, k_{\mathrm{B}}T/\mu\mathrm{m}^2$. Reported error bars are standard errors of the mean. Inset: Diffusion coefficient versus domain radius (circles) for 103 trajectories. The squares represent binned data. For comparison, the dashed-dotted line gives the behavior of $D(r)\, k_{\mathrm{B}}T/(16\eta r)$, which holds if the viscosity of water ($\eta \approx 10^{-3}\ \mathrm{Ns/m}^2$) is dominant [114]. The gray solid line shows a fit to the model described in [115] which gives $\eta' = 4.8 \times 10^{-8}\ \mathrm{Ns/m}$ for the 2D membrane viscosity. Reported error bars are standard errors of the mean.

5.4.3 Model for the spring constant

Due to the fact that the membrane of a GUV is both curved and finite in size, the calculation of the interaction potential between two distortions on such a membrane is a very difficult task. However, in the case where we are dealing

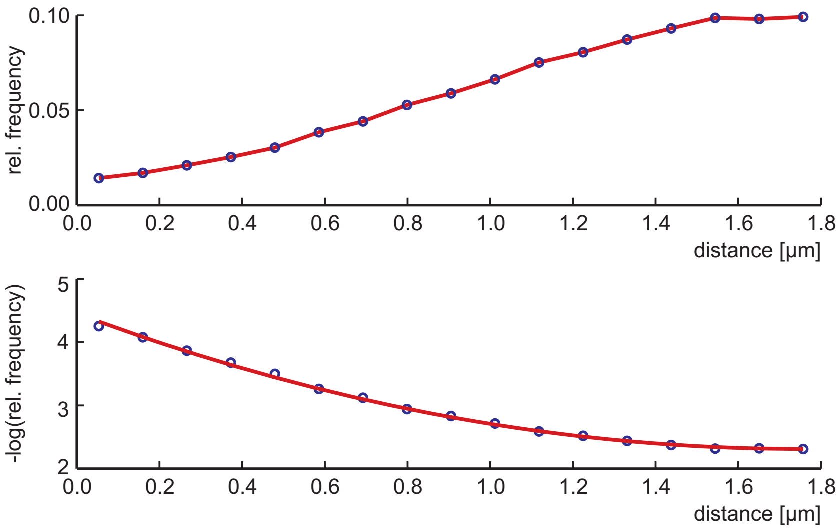

Figure 5.8: Spring constant k determined by domain distance statistics. Upper plot: relative frequency of edge-edge distances; lower plot: -log(rel. frequency) with fit to harmonic potential (solid line).

with a large number of small domains on a big vesicle the situation approaches that of domains on an infinite and asymptotically flat membrane. For two such domains with the shape of spherical caps, the interaction potential was first calculated by Goulian *et al.* [97] and reads

$$V = 4\pi\kappa(\alpha_1^2 + \alpha_2^2)\left(\frac{a}{r}\right)^4 \tag{5.14}$$

where r is the center-to-center distance between the two domains, a is a cut-off lengthscale taken to be the membrane thickness (a few nanometers), α_1 and α_2 are the domain's contact angles with the surrounding membrane (see figure 5.5d) and κ is the bending modulus of the background membrane. In appendix 5.C we give a derivation of equation (5.14), based on a calculation by Dommersnes and Fournier [99]. In order to be able to use equation (5.14) in our system, we again assume that the domains are nondeformable spherical caps. Because the ratio of the bending modulus of the L_o domains with that of the surrounding L_d membrane is significantly larger than 1 ($\kappa_\mathrm{o}/\kappa_\mathrm{d} \approx 4$, see chapter 4), this spherical cap approximation is valid.

As Dommersnes and Fournier showed [99], the interaction between multiple inclusions is not equal to the sum of their pairwise interactions. However, the scaling of the interaction with the distance between the domains r and the contact angles α_i does not change, only the prefactor does. For any budded domain surrounded by several other budded domains, we can therefore assume a potential of the form

$$V = \bar{C} \kappa a^4 \sum_{i=1}^{N} \frac{\alpha_0^2 + \alpha_i^2}{r_{0i}^4}, \tag{5.15}$$

where $\bar{C}$ is a numerical constant (which can be determined numerically using the method described in appendix 5.C), α_0 the contact angle of the domain we are interested in, α_i that of the ith neighbor and r_{0i} the distance between the central domain and its ith neighbor. The number of neighbors is N, which in experimental vesicles is typically 5 or 6, corresponding to a relatively dense packing of domains. Let us assume for simplicity that the equilibrium of the potential (5.15) is such that the nearest neighbors form a circle of radius r_0 around it, on which they are on average equally distributed (see figures 5.2 and 5.1a). This mean field assumption means that the central domain sees its environment as isotropic (it is not pushed in any particular direction) and its potential has a unique global minimum at the center of the circle. The energy of any displacement Δr of the central domain away from its energy minimum can then be calculated by an expansion in Δr of (5.15). The linear term in that expansion vanishes because of the isotropic distribution of the neighbors, in agreement with the assumption of the existence of a global potential minimum at $\Delta r = 0$. The first term of interest is therefore the quadratic term, which is given by

$$V_{\text{quadratic}} = \frac{C \kappa a^4}{2} \frac{\alpha_0^2 + \beta^2}{r_0^6} (\Delta r)^2, \tag{5.16}$$

where C is another constant and β the contact angle of a neighboring domain that would correspond to the time-average isotropic potential assumed above. Equation (5.16) allows us to experimentally determine the strength of the interactions between budded domains, since it yields an effective spring constant which can be measured:

$$k = C \kappa a^4 \frac{\alpha_0^2 + \beta^2}{r_0^6}. \tag{5.17}$$

In order to be able to predict the behavior of the spring constant k as a function of the domain size d (the length of its projected radius), we need to establish how α and r_0 vary with d. At present we have no way of determining $\alpha(d)$ from first principles, since that would require having a full description of the complete vesicle membrane. We can argue though that at least it should be an increasing function of d for small domains. When a domain has just grown large enough to bud out, its circumference will still be small, and the amount of membrane bending and stretching it can induce to reduce the line tension term will also be small. As the domain grows in size, this balance shifts, and by budding out further the domain makes its presence felt more strongly in the surrounding membrane. Because in our experimental system we always consider vesicles with many small domains, we assume $\alpha(d)$ to be in the linear regime. We therefore phenomenologically write: $\alpha \propto (d - d_0)$, where d_0 is the domain size at which budding first occurs, which should be of the order of the invagination length ($0.5 - 1.0$ μm, see section 5.3).

For $r_0(d)$ we do not need to make a guess, but can simply rely on experimental results, which show that r_0 depends linearly on d (figure 5.6b). Finally we will assume that $\alpha_0 \sim \beta$, since in experiments we typically find that domains are surrounded by domains of approximately equal size (see chapter 6). Using the linear dependencies of α_0 and r_0 on d in the expression for the spring constant (5.17), we find

$$k = A\frac{(d - d_0)^2}{(\bar{r}_0 + cd)^6}. \tag{5.18}$$

Equation (5.18) has two fitting parameters (A and d_0). The best fit of the experimental data is given by the dark gray solid line in figure 5.9. We find $A = 1.5 \times 10^5\ k_B T \mu\mathrm{m}^2$ and $d_0 = 0.55$ μm, which indeed is approximately the size of the invagination length (0.7 μm). Qualitatively we find that due to the increase in repulsion strength with growing domain size the spring constant increases with domain size for small domains. For very large domains on the other hand the interdomain distance also grows, and because the interactions fall off very steeply with distance, the spring constant decreases. In between we find a maximum that corresponds to the most abundantly present domain size in the experimental vesicles.

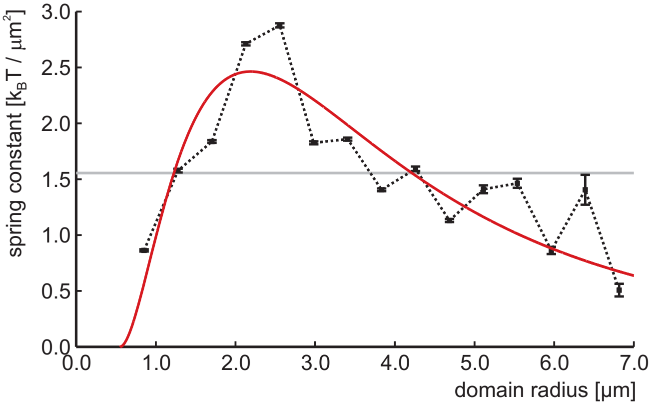

Figure 5.9: Effective spring constant k versus domain radius (circles), the squares correspond to binned data. The light gray solid line marks the average $k = 1.6 \pm 0.2\ k_B T/\mu\mathrm{m}^2$ and the dark gray solid line the theoretical fit determined using equation (5.18).

5.5 Conclusion

The experimental results on vesicles with many domains demonstrate the existence of membrane mediated interactions between them. In this chapter we have quantified the strength of these interactions. We have shown that they originate in the curvature the domains locally impose on their environment. We have also shown that the phenomenon of partial domain budding can be explained as a competition between curvature and elastic forces on the one hand and tensile forces on the other hand. Furthermore, we found that the membrane mediated interaction influences the fusion behavior of domains, resulting in a preferred domain size. Using a simple Monte Carlo simulation we were able to reproduce the experimental domain size distribution. Finally we found that the dependence of the interaction strength on distance is consistent with existing theory, which gives a $1/r^4$ dependence.

Proteins in the membranes of living cells distort their surrounding membrane in the same fashion as lipid domains do. We therefore predict that similar membrane mediated interaction forces play a significant role in membrane structuring. Coarse grained simulations show that membrane mediated interactions can lead to the aggregation of membrane inclusions [103]. In our experiments we do not observe such attracting behavior, which suggests that our model system is more comparable to larger structures, like protein aggregates. We expect that such aggregates experience repulsive interactions if they impose a curvature on the membrane. If this curvature exceeds a certain critical size the aggregates will not be able to grow further, just like the domains stop growing after reaching a certain size. Moreover, the membrane mediated interactions have a longer range ($1/r^4$) than Van der Waals interactions ($1/r^6$) and should therefore be the dominant interaction effect in the absence of electrical charges. We therefore expect this interaction to play an important role in many biological processes.

5.A Domain growth by aggregation: master equation description

The traditional starting point for treating aggregation is the infinite set of equations that describe how the cluster size (or ‘mass’) distribution changes with time. They are originally due to Smoluchowski, and the master equation below is the discrete version of Smoluchowski coagulation equation [116]. ‘Discrete’ here refers to the domain sizes (areas), we assume the concentration $c_k(t)$ of domains with size k to be a continuous function, *i.e.*, we assume the number of domains to be large. We denote the reaction rate of domains with size i and

j by K_{ij}. The master equation for $c_k(t)$ is then given by:

$$\dot{c}_k(t) = \frac{1}{2} \sum_{i+j=k} K_{ij} c_i(t) c_j(t) - c_k(t) \sum_{i=1}^{\infty} K_{ij} c_i(t), \tag{5.19}$$

where the dot denotes a derivative with respect to time. The first term of (5.19) describes the gain in the concentration of domains of size $k = i + j$ due to the coalescence of a domain of size i with a domain of size j. The rate at which this aggregation process occurs is $K_{ij} c_i(t) c_j(t)$; the product $c_i(t) c_j(t)$ gives the rate at which the domains meet, and the reaction kernel K_{ij} is the rate at which domains actually coalesce when they encounter each other. The second (loss) term of (5.19) accounts for the loss of domains of size k due to their reaction with clusters of arbitrary size i. The prefactor of $1/2$ in the gain term ensures the correct counting of their relative contributions.

An important feature of equation (5.19) is that the total mass is conserved:

$$\sum_k k\dot{c}_k = \sum_k \sum_{i+j=k} \frac{1}{2} K_{ij}(i+j) c_i c_j - \sum_i \sum_k K_{ik} k c_i c_k = 0. \tag{5.20}$$

In the first term of (5.20), the sum over k causes the sums over i and j to become independent and unrestricted. Thus the gain and loss terms become identical and the total mass is conserved.

In the literature, exact solutions of (5.19) are known for three different kernels K_{ij}: $K_{ij} = \text{constant}$, $K_{ij} = i + j$, and $K_{ij} = ij$, or the constant, sum and product kernel respectively [116–119]. Here we will give the solution for the constant kernel (where we set $K_{ij} = 2$ for convenience). It shows that, when starting from an initial system of monomers (all domains equal in size), we arrive at an exponential distribution of domain sizes over time. For $K_{ij} = 2$, the master equation (5.19) reads

$$\dot{c}_k = \sum_{i+j=k} c_i c_j - 2c_k \sum_{i=1}^{\infty} \equiv \sum_{i+j=k} c_i c_j - 2c_k N, \tag{5.21}$$

where N is the zeroth moment of the mass distribution

$$N(t) = \sum_{i=1}^{\infty} c_i(t), \tag{5.22}$$

i.e., the concentration of clusters of any mass i. The monomer-only initial condition means that we set $c_k(t=0) = \delta_{k,0}$. Because the master equation (5.21) for $c_k(t)$ depends only on $c_i(t)$ with $i \leq k$, we can solve these equations one by one by starting from $i = 1$, if we can determine $N(t)$ separately. To do so, we sum (5.21) over all k and find

$$\dot{N} = -N^2, \tag{5.23}$$

of which the general solution is given by

$$N(t) = \frac{N(0)}{1 + N(0)t} \to \frac{1}{t} \text{ as } t \to \infty. \tag{5.24}$$

Equation (5.24) tells us that $N(t)$ does not depend on the initial concentration $N(0)$ as $t \to \infty$. Moreover, combining equations (5.20) and (5.24), we find that in this limit the average mass of a domain grows linearly in time.

As stated, we can now progressively find $c_k(t)$ from (5.21) by substituting $N(t)$ from (5.24) and $c_i(t)$ for $i < k$ and integrating directly. Doing so, we find $c_1(t) = 1/(1+t)^2$ and $c_2(t) = t/(1+t)^3$. However, we can also solve for all $c_k(t)$ at once by rescaling (5.21). To do so, we write

$$\dot{c}_k + 2c_k N = \sum_{i+j=k} c_i c_j. \tag{5.25}$$

We introduce the integrating factor

$$I = \exp\left[2 \int^t N(t')\,\mathrm{d}t'\right] = (1+t)^2, \tag{5.26}$$

and define $\phi_k = c_k I$. We also define a rescaled time variable by $\mathrm{d}x = \mathrm{d}t/I(t)$, or explicitly

$$x = \int_0^t \frac{\mathrm{d}t}{(1+t)^2} = \frac{t}{1+t}. \tag{5.27}$$

Writing (5.25) in terms of $\phi_k(x)$, we get the simple expression

$$\phi'_x = \sum_{i+j=k} \phi_i \phi_j, \tag{5.28}$$

where the prime denotes a derivative with respect to the new time variable x. Effectively we have rewritten (5.21) such that there are only gain terms. The solutions of (5.28) are given by $\phi_k = x^{k-1}$ up to a scaling factor. From the explicit solutions of $N(t)$ and $c_1(t)$ we find $\phi_1 = 1$. Using (5.26) and (5.27), we find the exact solution of (5.21)

$$c_k(t) = \frac{t^{k-1}}{(1+t)^{k+1}} \to \frac{1}{t^2} e^{-k/t} \text{ as } t \to \infty. \tag{5.29}$$

The solution (5.29) decays very quickly over time for any k, and all $c_k(t)$ in fact approach a common limit that decays as $1/t^2$ as $t \to \infty$. Moreover, for fixed time, we find that the distribution of domains decays exponentially with their size k.

5.B Monte Carlo simulations of the domain size distribution

In this appendix we study domain growth by aggregation using Monte Carlo simulations. We simulate both the case described in appendix 5.A, where domains fuse upon encounter, and the case in which the fusion rate depends on the domain sizes (or masses). For the size-independent fusion rate, equation (5.29) gives the exact solution for $c_k(t)$, the concentration of domains of size k at time t, assuming we start with a monodisperse set of domains of size 1. The exponential decay of $c_k(t)$ with k for fixed t is reproduced by the Monte Carlo simulations. When we introduce a size dependence in the fusion rate, we find that the decay time becomes much longer, and that the distribution for small sizes deviates from the exponential distribution. Since both are found in experiments, they are a clear indication that an interaction is present.

Like in appendix 5.A, we assume that the rate $k_{i,j}$ for the fusion of two domains of size (*i.e.*, area) i and j can be written as the product of two factors: the rate for random encounter by diffusion $k_{\text{diff}}(\{c_k\})$, which may depend on the distribution of domain sizes $\{c_k\}$, and the probability $p_{i,j}^{\text{merge}}$ for domain merger if the domains are close to each other:

$$k_{i,j} = p_{i,j}^{\text{merge}} k_{\text{diff}}(\{c_k\}). \tag{5.30}$$

In our simulations we start with $1/\varepsilon$ domains of size ε. During the simulation the domains are fused randomly with the rates $k_{i,j}$ given by (5.30). The fusion rate is converted to a fusion probability $p_{i,j}$ by multiplication with a small time step Δt. Since there are $\frac{1}{2}n(n-1)$ possible pairings of n domains we write the fusion probability $p_{i,j}$ as:

$$p_{i,j} = k_{i,j}\Delta t = \frac{1}{\frac{1}{2}N(N-1)} p_{i,j}^{\text{merge}} \left(\frac{1}{2}N(N-1)\right) k_{\text{diff}}(\{c_k\})\Delta t, \tag{5.31}$$

where the total number of domains is given by $N(t) = \sum_k c_k(t)$. If the time step Δt is chosen to be $\Delta t = \left[(\frac{1}{2}N(N-1))k_{\text{diff}}(\{c_k\})\right]^{-1}$, the fusion probability becomes

$$p_{i,j} = \frac{1}{\frac{1}{2}N(N-1)} p_{i,j}^{\text{merge}}. \tag{5.32}$$

The Monte Carlo algorithm we use is detailed in [120]. Briefly, in each Monte Carlo step, first a pair of domains is chosen randomly and the Monte Carlo time is increased by Δt. With a probability of $p_{i,j}^{\text{merge}}$ the domain fusion is executed.

In agreement with our experimental observations we do not allow for scission events, *i.e.*, the fission of a domain into two smaller domains. Due to the high line tension such events never occur in our experiments.

In order to take the spatial distribution and diffusion of domains into consideration, we adopt the scaling argument used in [93] and [106]. The time τ_{diff} for two domains to encounter each other at random due to diffusion scales like $\tau_{\text{diff}} \propto \langle r^2 \rangle / D(r)$, with r the domain radius and $D(r)$ the diffusion constant. Since we observe only a weak dependence of the diffusion coefficient on domain size ($D(r) \approx D$, see inset of figure 5.7), we set $k_{\text{diff}}(\{c_k\}) = \pi / \langle A \rangle$ with the average domain area $\langle A \rangle = \frac{1}{N} \sum_k k c_k$. This rate should give the correct time scale for domain fusion apart from a constant prefactor. To gauge the simulations with real experimental time scales, we let the system evolve to complete phase separation for non-interacting domains ($p_{i,j}^{\text{merge}} = 1$) and compare the resulting Monte Carlo time to measured time scales. In the case of (flat) domains, which are free to fuse, the time needed for complete separation was determined experimentally (see [106], normal coarsening) and is about 1-10 minutes. The corresponding Monte Carlo time in our simulations is $T_{\text{MC}} \approx 2$. Figure 5.4b shows intermediate domain size distributions for four different Monte Carlo times. Clearly, the exponential behavior is conserved in the presence of diffusion and the typical lengthscale of that distribution (*i.e.*, domain size) increases over time.

In the kinetic hindrance model for budded domains the probability for merger of two neighboring domains decreases with domain size. Since we do not attempt to obtain quantitative agreement with the experimental results, we can use any probability that decreases monotonically with domain size. We have performed simulations with both $p_{i,j}^{\text{merge}} = c/\sqrt{i * j}$ and $p_{i,j}^{\text{merge}} = c/(i * j)$. The results are presented in figure 5.4c and d respectively, showing intermediate domain size distributions for 4 different Monte Carlo times. The simulations reproduce the two qualitative features observed in experiments: the local maximum and the exponential tail, see figure 5.3. We find that for $T_{\text{MC}} > 100$ phase separation is still not complete. The process thus takes much longer than the time we found for complete phase separation in the case without interactions ($T_{\text{MC}} \approx 2$). The Monte Carlo simulations therefore show that microphase separation is a quasistatic state, confirming the result of section 5.3 (see also figure 5.5f).

5.C Interaction potential

For two conical inclusions (with spherical cross section), the membrane-mediated interaction potential (5.14) was first calculated by Goulian, Bruinsma, and Pincus [97], using variational calculus. Here we follow a construction by Dommersnes and Fournier [99], using an expansion in small deformations and a Green's function description, to get the potential for an arbitrary number of inclusions.

In this calculation, we assume the membrane to be infinitely large and asymptotically flat. We also assume the membrane to be uniform and tensionless, such that the only contribution to the energy is the mean curvature term of the Canham-Helfrich energy (2.78). We assume there are only small deviations $u(x,y)$ from the (x,y) plane, and there are no overhangs, ***i.e.***, $u(x,y)$ is well-defined for any point (x,y). These assumptions allow us to use the Monge gauge, in which we write $\vec{r} = (x, y, u(x,y))$. The free energy then reads in terms of u:

$$\mathcal{E} = \frac{\kappa}{2} \int \left(\nabla^2 u\right)^2 \mathrm{d}x\,\mathrm{d}y, \tag{5.33}$$

where κ as usual is the bending modulus of the membrane, and $\vec{\nabla} = (\partial_x, \partial_y)$ the differential operator on $\mathbb{R}^2$. We next put our N inclusions in the membrane at positions which we label $\vec{r}_k$, with $k = 1, \ldots, N$. The task at hand is to minimize (5.33) given the boundary conditions we thus impose at the points $\vec{r}_k$. These boundary conditions fix the local curvature tensor at $\vec{r}_k$. In the small deformation limit, the elements of that tensor are given by the second derivatives of the membrane shape, so by $\partial_{xx}u(\vec{r})$, $\partial_{xy}u(\vec{r})$ and $\partial_{yy}u(\vec{r})$. We fix the curvature constraints using $3N$ Lagrange multipliers Λ^k_{ij}. The Euler-Lagrange equations for the constrained minimization of (5.33) then read:

$$\nabla^2\nabla^2 u(\vec{r}) = \sum_{k=1}^{N} \left[\Lambda^k_{xx}\partial_{xx}\delta(\vec{r}-\vec{r}_k) + \Lambda^k_{xy}\partial_{xy}\delta(\vec{r}-\vec{r}_k) + \Lambda^k_{yy}\partial_{yy}\delta(\vec{r}-\vec{r}_k)\right], \tag{5.34}$$

with $\delta(\vec{r})$ the two-dimensional Dirac delta function. Because equation (5.34) is linear, we can write the general solution as a linear combination of derivatives of the Green's function of the operator $\nabla^2\nabla^2$. The solution is given by

$$u(\vec{r}) = \sum_{m=1}^{3N} \Lambda_m \Gamma_m(\vec{r}), \tag{5.35}$$

with

$$\Lambda = \begin{pmatrix} \Lambda^1_{xx} \\ \Lambda^1_{xy} \\ \Lambda^1_{yy} \\ \Lambda^2_{xx} \\ \vdots \end{pmatrix}, \qquad \Gamma(\vec{r}) = \begin{pmatrix} \partial_{xx}G(\vec{r}-\vec{r}_1) \\ \partial_{xy}G(\vec{r}-\vec{r}_1) \\ \partial_{yy}G(\vec{r}-\vec{r}_1) \\ \partial_{xx}G(\vec{r}-\vec{r}_2) \\ \vdots \end{pmatrix}. \tag{5.36}$$

The Green's function is given by

$$G(\vec{r}) = \frac{1}{16\pi} r^2 \log r^2, \tag{5.37}$$

with $r = |\vec{r}|$, satisfying $\nabla^2\nabla^2 G(\vec{r}) = \delta(\vec{r})$. We group the values of the $3N$

constraints in a column matrix K:

$$K = \begin{pmatrix} \partial_{xx} u(\vec{r}_1) \\ \partial_{xy} u(\vec{r}_1) \\ \partial_{yy} u(\vec{r}_1) \\ \partial_{xx} u(\vec{r}_2) \\ \vdots \end{pmatrix}. \tag{5.38}$$

The values of the Lagrange multipliers are set by the constraints in the $3N$ equations

$$\sum_{n=1}^{3N} M_{mn} \Lambda_n = K_m, \tag{5.39}$$

where M is the $3N \times 3N$ matrix

$$M = \begin{pmatrix} m_{11} & m_{12} & \cdots & m_{1N} \\ m_{21} & m_{22} & & \vdots \\ \vdots & & \ddots & \vdots \\ m_{N1} & \cdots & \cdots & m_{NN} \end{pmatrix}, \tag{5.40}$$

in which the m_{ij}'s are the 3×3 matrices given by

$$m_{ij} = \begin{pmatrix} \partial_{xxxx} G(\vec{r}_{ij}) & \partial_{xxxy} G(\vec{r}_{ij}) & \partial_{xxyy} G(\vec{r}_{ij}) \\ \partial_{xxxy} G(\vec{r}_{ij}) & \partial_{xxyy} G(\vec{r}_{ij}) & \partial_{xyyy} G(\vec{r}_{ij}) \\ \partial_{xxyy} G(\vec{r}_{ij}) & \partial_{xyyy} G(\vec{r}_{ij}) & \partial_{yyyy} G(\vec{r}_{ij}) \end{pmatrix}, \tag{5.41}$$

with $\vec{r}_{ij} = \vec{r}_i - \vec{r}_j$. Integrating equation (5.33) by parts, while taking into account the constraints (5.38), gives for the elastic energy

$$\mathcal{E} = \frac{\kappa}{2} K^T M^{-1} K, \tag{5.42}$$

where K^T is the transpose of K. From equations (5.35) and (5.39) we find for the equilibrium shape of the membrane

$$u(\vec{r}) = K^T M^{-1} \Gamma(\vec{r}). \tag{5.43}$$

To get explicit expressions, we write

$$\vec{r}_{ij} = \vec{r}_i - \vec{r}_j = r_{ij} (\cos\theta_{ij} \hat{x} + \sin\theta_{ij} \hat{y}), \tag{5.44}$$

which gives for m_{ij} in case $i \neq j$

$$m_{ij} = \frac{1}{4\pi r_{ij}^2} \begin{pmatrix} \cos(4\theta_{ij}) - 2\cos(2\theta_{ij}) & \sin(2\theta_{ij}) \cdot (2\cos(2\theta_{ij}) - 1) & -\cos(4\theta_{ij}) \\ \sin(2\theta_{ij}) \cdot (2\cos(2\theta_{ij}) - 1) & -\cos(4\theta_{ij}) & -\sin(4\theta_{ij}) - \sin(2\theta_{ij}) \\ -\cos(4\theta_{ij}) & -\sin(4\theta_{ij}) - \sin(2\theta_{ij}) & \cos(4\theta_{ij}) + 2\cos(2\theta_{ij}) \end{pmatrix}. \tag{5.45}$$

For $i = j$, the expression (5.45) for m_{ij} diverges. This divergence is due to the fact that the energy (5.33) is a coarse-grained description which is only valid for distances $r \leq r_0$, with r_0 the membrane thickness. We should therefore introduce a cutoff in the theory at high wavevector of order $1/r_0$, which will allow us to calculate m_{ij} for $i = j$. To do so, we consider the derivatives of the Green's function (5.37) in Fourier space; for example

$$\partial_{xxxx} G(\vec{r}\,) = \frac{1}{(2\pi)^2} \int \frac{q_x^4}{q^4} e^{i\vec{q}\cdot\vec{r}} \, \mathrm{d}^2 q, \tag{5.46}$$

where $\vec{q} = (q_x, q_y)$ and $q = |\vec{q}\,|$. Introducing the high wavevector cutoff, we find

$$\partial_{xxxx} G(\vec{0}\,) = \frac{1}{(2\pi)^2} \int_0^{1/r_0} q \, \mathrm{d}q \int_0^{2\pi} \cos^4\theta \, \mathrm{d}\theta = \frac{3}{32\pi r_0^2}, \tag{5.47}$$

and similarly for the other matrix elements of (5.41). The entire matrix m_{ii} is given by

$$m_{ii} = \frac{1}{32\pi r_0^2} \begin{pmatrix} 3 & 0 & 1 \\ 0 & 1 & 0 \\ 1 & 0 & 3 \end{pmatrix}. \tag{5.48}$$

To recover the result by Goulian *et al.*, we consider two identical isotropic inclusions, each prescribing the curvature c. The matrix of constraints then reads

$$K^T = (c, 0, c, c, 0, c). \tag{5.49}$$

The elastic energy is now given by equation (5.42)

$$\mathcal{E} = \frac{512\pi\kappa(r_0 c)^2}{\left(\frac{R}{r_0}\right)^4 + 8\left(\frac{R}{r_0}\right)^2 - 32}, \tag{5.50}$$

where $R = r_{12}$ and we have discarded a constant term. Setting $r_0 = a/2$, and making an expansion around $R = \infty$, we find

$$\mathcal{E} = 8\pi\kappa(ac)^2 \left(\frac{a}{R}\right)^4 + \mathcal{O}\left(\frac{1}{R}\right)^6, \tag{5.51}$$

which is the result of Goulian *et al.* [97]. Using this formalism we can find the energy for any number of inclusions. The only limitation is that we have to invert the $3N \times 3N$ matrix M_{ij}. As Dommersnes and Fournier showed by an explicit calculation for a three particle system [99], the potential is not pairwise additive, however the dependence

$$V = \bar{C}\kappa a^4 \sum_{i=1}^{N} \frac{\alpha_0^2 + \alpha_i^2}{r_{0i}^4}, \tag{5.52}$$

given by equation (5.15) holds, and the constant $\bar{C}$ can be determined numerically.